Alignment Maps of Tissues: I. Microscopic Elliptical Polarimetry

Theodore T. Tower and Robert T. Tranquillo
Department of Chemical Engineering & Materials Science, University of Minnesota, Minneapolis, Minnesota 55455 USA

ABSTRACT An automated method for generating a fiber alignment map in tissues, tissue-equivalents, and other fibrillar materials exhibiting linear and circular optical properties and scattering is presented. This method consists of interrogating the sample with elliptically polarized light from a rotated quarter-wave plate and an effective circular analyzer, and implementing nonlinear regression techniques to estimate parameters defining the optical properties of the optic train and the sample. Thus, an account is made for imperfect and misaligned optic elements. The optic train was modeled using the Mueller matrix representation and the combined sample properties by an exponential matrix. Because a sample's Mueller matrix does not uniquely determine the linear, circular, or scattering properties, the circular properties and effective scattering are estimated for a matched isotropic sample to determine and correct for the linear birefringence of an aligned sample. The method's utility is demonstrated by generating an alignment map of an arterial media-equivalent, a relevant test case because of its circumferential alignment and thus showing the method's sample orientation independence.

INTRODUCTION

Soft connective tissues can be modeled as biphasic materials composed of a network of fibers (pre-dominantly collagen) and an isotropic, though chiral, interstitial fluid. Tissues with nearly uniaxial alignment of fibers, such as ligaments and tendons, may be characterized by a single alignment angle and strength of alignment; but, in general, tissues have an alignment pattern and possess complex geometries, which requires a method that generates a spatial map of alignment. These patterns can be used to characterize healing tissue, track normal development and growth of tissue, and discriminate healthy from pathological tissue (Thomsen et al., 1989). Generating fiber alignment maps of native and artificial soft connective tissues would facilitate a goal of biomechanics to relate fiber alignment to tissue mechanical properties. Progress would be aided by an efficient, automated method for generating maps of fiber alignment that is accessible to the general researcher and is noninvasive and nondestructive.

Although a full three-dimensional (3D) alignment map is necessary to characterizer the fiber structure when it varies across the thickness of the tissue, this is difficult to acquire, and a two-dimensional (2D) map often suffices. Polarized light microscopy is attractive for generating 2D alignment maps because it is a noninvasive, submicroscopic method; even though the network itself often cannot be resolved, the net optical properties that are imaged reflect the nature of the microstructure. However, the measured image intensity is due to the contribution of many species and the ways they may affect the resulting polarization state. Linear optical properties, namely linear birefringence (LB) and dichroism (LD) are associated with overall fiber alignment. We define an alignment map based on spatial variation of the sample retardation, δ, the extensive quantity related to the true intensive birefringence, LB, and the alignment direction, χ. Chiral molecules, such as common solutes found in the interstitial fluid, and the collagen fibers themselves, exhibit circular optical properties, namely circular birefringence (CB) and dichroism (CD), though, normally, at magnitudes much smaller than their linear counterparts.

Additionally, there may be significant scattering by the various species present, including Rayleigh scattering by particles smaller than the wavelength of light. The scattering process itself introduces a polarization of the incident light, termed s-polarized light (i.e., linearly polarized in a plane normal to the scattering plane, see Fig. 1 *A*) (van de Hulst, 1957; Brosseau, 1998). The imaging system objective collects the unscattered incident light and the scattered light that falls within the solid angle defined by its numerical aperture (Finzi et al., 1991). For incident unpolarized light, the net effect is that s-polarized light, when averaged over all polar angles, results in an unpolarized contribution to the measured intensity (see Fig. 1 *B*). For incident polarized light, the effect of Rayleigh scattering depends on the polarization state of the incident wave. For example, vertical polarized light is most strongly scattered in the horizontal plane, retaining its vertical polarization, and scatters the least in the vertical direction, where there is no horizontal component to the incident light, yielding a scattering contribution to the measured intensity that is vertically polarized in nature (see Fig. 1 *C*). In contrast, incident circularly polarized light results in s-polarized scattered light uniformly over all polar angles, yielding a scattering contribution with no net polarization (i.e., unpolarized). Techniques that use large numerical apertures, such as microscopes and modulated polarization states, must account for the scattering polarization bias.

Received for publication 22 December 2000 and in final form 29 May 2001.

Address reprint requests to Robert T. Tranquillo, Dept. of Biomedical Engineering and Chemical Engineering & Materials Science, Univ. of Minnesota, 151 Amundson Hall, 421 Washington Ave., SE, Minneapolis, MN 55455. Tel.: 612-625-6868; Fax: 612-626-7246; E-mail: tranquillo@cems.umn.edu.

0006-3495/01/11/2954/10 $2.00

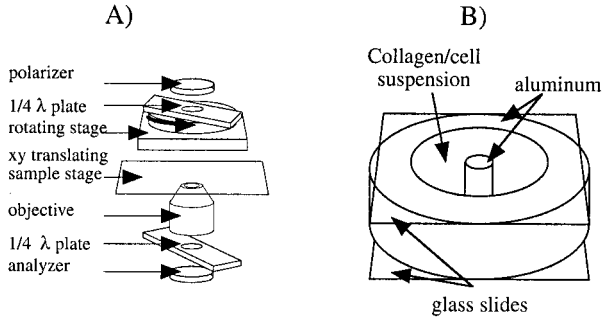

FIGURE 1 Polarization of scattered light. (*A*) Point scatterers scatter incident unpolarized light perpendicular to the scattering plane (s-polarized) with only a single (horizontal) scattering plane of the scattering enveloped being illustrated. The degree of the s-polarization is greatest in the direction perpendicular to the incident light, and decreases with increasing forward or backward scattering. (*B*) An imaging system collects the undeviated incident light (as shown in center) and a cone of the forward-scattered s-polarized light (shown as rays to the edges of the objective). The scattered light, averaged over all polar angles, results in no net polarization. (*C*) With incident linear polarized light, the measured intensity will result of the undeviated linear polarized light and a partially linear polarized component. (*D*) With incident circularly polarized light, the measured intensity will result from a combination of the undeviated circular polarized light and the unpolarized polar-average contribution of the scattered light.

Although traditional polarized light microscopy relied on rotation of the sample to see its effect on a given incident polarization light (Guido and Tranquillo, 1993; Osaki, 1994; Bear and Schmitt, 1936), most modern orientational spectroscopy and photometric methods use a modulated probe or analyzer, changing the ellipticity of the illuminating light and extracting a particular polarization component of the resultant light vector. One simple yet powerful approach to yield individual images of the elements of the Mueller matrices is by the manual insertion of optical elements to perform the differential polarization imaging described by Bustamante and coworkers (Kim et al., 1987). More attractive are automated methods of acquiring sample optical properties, including rotation of the polarizer (Glazer et al., 1996; Geday et al., 2000) or a λ/4 plate (Hauge, 1978), or using a photoelastic modulator. In recent years, photoelastic modulators have received the most attention because of their speed and absence of moving parts. Oldenbourg and Mei (1995) incorporated these elements into the commercial PolScope (Cambridge Research & Instrumentation, Inc.,) using a "universal compensator," which rapidly generates a pixel-wise alignment map for weakly aligned specimens that act as linear retarders.

Despite the extensive use of modulated probes, there has not been extensive development of methods that account for combined linear, circular, and scattering optical properties that are inherent with tissues. We address this deficiency using the Mueller calculus, where a sample's 4×4 Mueller matrix completely describes how the incoming polarization state of light is transformed by an optical element. However, the set of optical properties that lead to a given Mueller matrix are not unique (Schellman and Jensen, 1986). Methods that measure LB and LD (van Haeringen et al., 1994) operate under the assumption that circular properties are negligible (as they often are). For isotropic materials, other methods are well suited to characterize CB and CD (Hennessey and Johnson, 1982; Long and Urry, 1981). Most of these methods ignore the scattering function or choose a low numerical aperture to exclude it.

However, in general, linear, circular, and scattering components may all be significant, particularly in tissues that exhibit weak or developing alignment, such as tissues in developmental and wound-healing processes, artificial tissues being fabricated, or any tissue immersed in cell-culture medium. In these cases, the circular and scattering components must be taken into account to accurately measure the contribution of LB, which gives the fiber alignment map of interest. We are not aware of any methods capable of accurately measuring weak LB of tissue maintained in culture medium, both which contain chiral biological molecules exhibiting CB and CD, including chirally active sugars and proteins, and to account for the polarized scattering of turbid media. This is especially important when investigating changes in gel alignment during time-lapse experiments where the samples must remain viable over several hours on the microscope. To aid in the characterization of materials that exhibit multiple optical properties, Jones developed an approach by which a sample matrix may be generated from a line integral of differential elements (Jones, 1948). Complex samples may then be treated as series of differential linear and circular retarders and absorbers. This formalism has been extended to the Mueller calculus (Schellman and Jensen, 1986).

We present an inexpensive alternative to more sophisticated equipment by using a polarizer/rotating λ/4 plate as a modulated source and an effective circular analyzer to interrogate the sample. Image processing and nonlinear least squares regression of equations modeling the optic train and sample allows the generation of maps of important optical properties. To accurately assess a sample's LB map, and, hence, the fiber alignment map, the effective circular properties and scattering must be determined independently. By determining the circular and scattering components of the Mueller matrix from a matched isotropic sample and applying those constants to an aligned sample, we can generate an accurate LB map with our method. As a result, we have developed a powerful tool to generate alignment maps in tissues and fibrillar materials for which linear, circular, and scattering optical properties contribute significantly.

The method's usefulness is demonstrated by the generation of an alignment map of an arterial media equivalent (ME) fabricated by cell-induced compaction of a tube of type I collagen gel containing rat dermal fibroblasts around a mandrel. The compaction around a nonadhesive mandrel

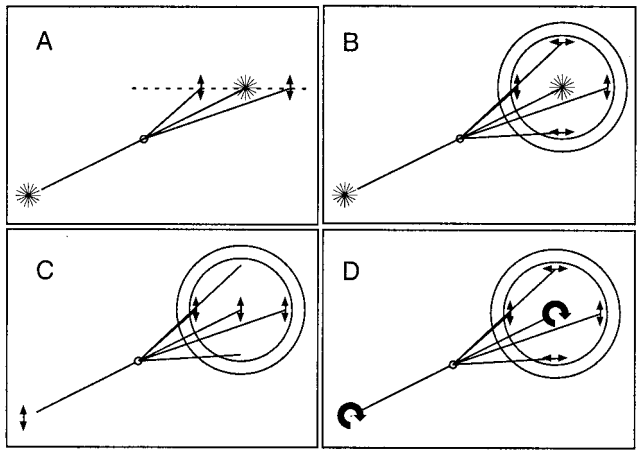

FIGURE 2 Optic train and media-equivalent sample chamber diagrams. (*A*) The optic train. (*B*) The sample chamber was filled with the collagen/cell suspension in the annular space between the glass slides.

leads to circumferential alignment of the cells and collagen fibrils (Barocas et al., 1998). This provides a relevant test case for demonstrating the method's utility on thick, turbid, biological samples and for confirmation that results do not depend on the sample alignment (since all alignments are represented in a circumferentially aligned sample). A similarly prepared cylinder of similar volume that compacted isotropically allowed the measurement of circular and scattering properties in the absence of linear properties. The estimates of the circular and scattering properties were used to deconvolve the linear properties for the ME, allowing the generation of an alignment map.

MATERIALS AND METHODS

Automated polarized microscope system

Experiments were performed with a research grade Olympus IX-70 inverted light microscope equipped with the following features: brightfield optics (4×, 10×, 20×, 40×), side-port mounted Photometrics SenSYS CCD digital camera (1317 × 1035 pixels, 12-bit grayscale, SCSI interface), halogen source, and monochromatic filter (546 nm). Motorized X–Y translating stage (Ludl), rotating stage (Oriel), and light shutters were controlled by a Ludl Electronic Products MAC 2000 controller. The Inovision dsp/os software running on a Silicon Graphics O2 provided direct control of image acquisition and sample positioning through operating-system-level commands accessed via custom Perl scripts. Nonlinear regression and standard statistical F-tests were performed by a user-written Fortran77 code.

The optic train described herein is shown in Fig. 2 *A*, with all angles relative to the fixed analyzer. The polarizer is followed by a λ/4 plate (slow axis initially at 45°) mounted to the motorized rotating stage. The tissue sample and the reference Brace–Kohler compensator (calibrated to 15.16 nm, and slow axis at 45°) (termed "reference" hereafter) were placed at different locations on the motorized X–Y stage. A second λ/4 plate (slow axis at 45°) was inserted in the slot beneath the objective, followed by a fixed analyzer (crossed to the polarizer).

Tissue sample

An arterial ME with strong circumferential alignment of collagen fibrils and cells was fabricated by compaction of a tube of type I collagen gel containing adult rat dermal fibroblasts (passage 7) around a nonadhesive mandrel as described in detail in Barocas et al. 1998). The collagen and cell suspension (10^6 cells/mL collagen solution) were put in aluminum annular chambers with a ⅝″ I.D. centered about a ¼″ O.D. aluminum post, both ½″ high (see Fig. 2 *B*), with glass slides on both ends. The chamber was incubated at 37°C for 1.5 h to allow gelation to occur. The ME originally had dimensions of the chamber, but compacted over 8 hours approximately 20% radially and longitudinally.

Image acquisition and post processing

Images were acquired using the Photometrics Sensys CCD camera. When both λ/4 plates are at 45°, they approximate a cumulative half wave retarder, rotating the linear polarization 90° from that of the polarizer to that of the analyzer, resulting in the maximum intensity being transmitted. The light intensity was adjusted to fit within the range of the CCD, requiring image exposure times typically 20–100 ms. A pixel binning of three was used to reduce noise and image size.

The λ/4 plate was rotated to 16 positions evenly spaced over 180°. To facilitate parallel acquisition of calibration and sample images, thus accounting for potential motor errors, we used X–Y stage automation to move the sample, the reference, and an empty field (termed "blank" hereafter), into the optic path for image acquisition at each λ/4 plate rotation angle. For large samples (several millimeters in size), image mosaics were generated by acquisition at 4× magnification in a raster pattern to cover the sample. Flat field correction was performed on each image. The sample image or mosaic at each λ/4 rotation angle was segmented into a grid of $n \times m$ subregions. Typically, using a 4× objective, a 20 × 20 alignment map sufficed for spatial resolution of the LB map of the ME. Finer grids may be used, down to a pixel-wise map (i.e. image), but the required computational time may be prohibitive. For both the spatially uniform blank and reference, a single mean grey level (MGL) was measured as a function of θ for calibration of the optic train.

MICROSCOPIC POLARIMETRY

The optic elements of the system depicted in Fig. 2 *A* and the sample were characterized by image acquisition through the three variants of the optical train (with the sample, reference, or the blank in the light path) as a function of the λ/4 plate rotation angle, θ, using the Mueller Matrix formalism in Eq. 1. The analyzer and polarizer were referenced according to their transmission axes by $P(0)$ and $P(90)$, respectively. The rotating and fixed position λ/4 plates and the reference are LB elements, with Mueller matrices, M_{LB}, and were characterized by a slow axis alignment, α, and retardation, ϕ. The attributes of the rotating λ/4 plate, the fixed λ/4 plate, and the reference are denoted by the subscripts r, f, and c, respectively. The Stokes vector for the incident unpolarized and resultant polarized light are s_{up} and s, respectively, using the Perrin order $[s_0 s_1 s_2 s_3]^T$ where s_0 is the total intensity, s_1 and s_2 are the 0°/90° and ±45° components of linear polarization, and s_3 is the circular component of polarization. Unless otherwise noted, letter subscripts are optic component references, and number subscripts refer to a matrix or vector element. Eq. 1 was used to

model the light intensities for the blank, reference, and sample, as a function of θ.

$$P(0)M_{\mathrm{LB,f}}(\alpha_{\mathrm{f}},\phi_{\mathrm{f}})MM_{\mathrm{LB,r}}(\alpha_{\mathrm{r}}+\theta,\phi_{\mathrm{r}})P(90)s_{\mathrm{up}}=s,$$

$$M=\begin{pmatrix} I & \text{blank} \\ M_{\mathrm{LB,c}} & \text{reference} \\ M & \text{sample} \end{pmatrix}. \quad (1)$$

To address the multiple optical properties exhibited by a sample, we use the Mueller matrix exponential formalism (Schellman and Jensen, 1986) to allow multiple properties to be combined in a single M. This allows the characterization of multiple optical properties that might be observed in an isotropic sample, such as CB, CD, and scattering, and to apply the associated values to M for an aligned sample of similar composition to determine LB, and hence, the alignment map. This is done by using the differential matrix, H, to generate the sample matrix, M, according to Eq. 2. Note that Eq. 2 is analogous to the familiar Beer–Lambert Law, where H is a polarization matrix form of the traditional absorption coefficient (Schellman and Jensen, 1986).

$$M=\exp(-H), \quad (2)$$

where, in the context of this paper, H is defined in

$$H=\begin{bmatrix} a & -ld_0 & -ld_{45} & cd \\ -ld_0 & a & cb & lb_{45} \\ -ld_{45} & -cb & a & -lb_0 \\ cd & -lb_{45} & lb_0 & a \end{bmatrix}, \quad (3)$$

where a is the isotropic absorption coefficient, ld_0, ld_{45} and lb_0, lb_{45} are the 0° and 45° components of the linear dichroism and birefringence, respectively, cb is the circular birefringence, and cd is the circular dichroism. The reader will note that the exponential form of Eq. 2 yields the usual Mueller matrices for absorption, LB, etc.

To statistically assess whether the sample exhibited any given optical property at an image subregion, the subregion's MGL(θ) was fit to Eq. 1 with a model of increasing complexity, where parameters' significance were determined by the F-test (significance level, $\alpha = 0.01$). First, the sample was assumed to be an isotropic absorber (with M equal to the identity matrix) and the intensities were fit with a scale and offset (two-parameter fit). The addition of optical properties to the model reduced the sum of squares error (SSE), which was translated to an F-value. If the critical F-value for significance was exceeded, determined by the degrees of freedom and significance level, the parameter statistically improved the model. The parameter with the largest F-score over the critical F, reducing the SSE the most, was retained as a model parameter, and by continuing this process, additional parameters were added in descending rank of importance to the model until no additional parameters were determined to be significant. There was some correlation between significant parameters, but ultimately the order of addition did not affect the values.

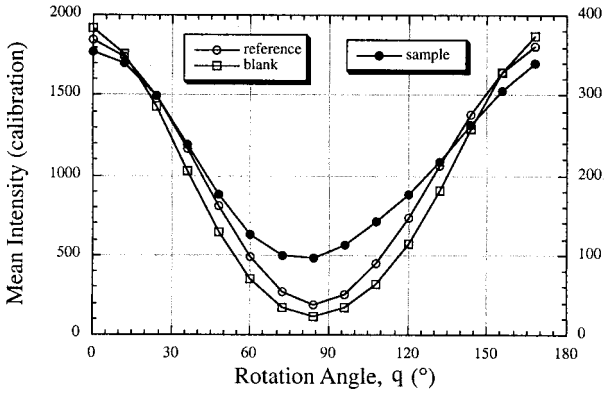

FIGURE 3 Intensity curves for sample, reference, and blank with a circular analyzer and rotating λ/4 plate. For all curves, the intensity maximum corresponds to both λ/4 plates (the rotating λ/4 plate and the effective circular analyzer), both being aligned at 45°, and the minimum to where they are crossed.

Calibration of optic train

Typical intensity curves, MGL(θ), and regression fits for a blank and reference are shown in Fig. 3. Calibration was done by simultaneous nonlinear least squares regression of the blank and reference curves to Eq. 1 using techniques outlined in Draper and Smith (1981). Given the known retardation of the reference, the other nine system parameters were fit: the scale and offset for the blank and reference curves (four parameters), the retardation and slow axes for both λ/4 plates (four parameters: α_{r}, α_{f}, ϕ_{r}, and ϕ_{f}), and the slow axis of the compensator (one parameter: α_{c}). The values of the parameters and the standard errors are reported in Table 1. Note that the retardations of the λ/4 plates differed significantly from 90°, because they were optimized for wavelengths apart from 546 nm. This demonstrates how imperfect elements may be used and corrected for in the analysis.

Isotropic samples

Isotropic samples, in general, may exhibit CB, CD, and scattering. A particle in solution will scatter a portion of an

TABLE 1 Regression parameters for optic train with their standard errors

Scale for reference	6527 ± 168
Offset for reference	83 ± 12
Scale for blank	6970 ± 185
Offset for blank	138 ± 7
α_{r}	49.1 ± 0.1
ϕ_{r}	75.1 ± 1.0
α_{f}	46.3 ± 0.4
ϕ_{f}	60.7 ± 2.1
α_{c}	65.9 ± 0.8

incident planar wavefront into a spherical wave eminating from the particle, whose polarization is dependent on both the polar and azimuthal angle. As a result, the sample Mueller matrix may have up to a full 16 nonzero elements. A common method to determine all 16 elements is the method described by Hauge (1978) using a rotating λ/4 plate before and after the sample. The rotating λ/4 plate after the sample serves to select which polarization state will be transmitted through the analyzer. We used a simplified approach, whereby, instead of using a rotating λ/4 plate after the sample, only two analyzer configurations were used: the analyzer alone and the effective circular analyzer by addition of a λ/4 plate at 45°. Determination of which elements of M were statistically nonzero was accomplished by simultaneous regression of the measured light intensity data from each analyzer combination.

For a demonstration of scattering from an isotropic medium, we compared cell-culture medium (M199, Gibco) and phosphate buffered saline (DPBS, Gibco). The saline exhibited no statistically significant birefringence, dichroism, or scattering, whereas the cell-culture medium was well characterized with nonzero entries in M along the diagonal, and where $m_{12} = m_{21}$. This is consistent with Rayleigh scattering with no circular birefringence, where the scattering matrix is given by (Brosseau, 1998)

$$M = \begin{bmatrix} m_{11} & m_{12} & 0 & 0 \\ m_{12} & m_{22} & 0 & 0 \\ 0 & 0 & m_{33} & 0 \\ 0 & 0 & 0 & m_{44} \end{bmatrix}. \quad (4)$$

Given a scale and offset, m_{12} was the most important to the model ($F_{(2,14),\alpha=0.01} = 123$, $F_{\text{critical}} = 6.51$). Using the matrix formalism of Eqs. 2 and 3, CB was determined to be an additional parameter of relatively minor importance ($F_{(3,13),\alpha=0.01} = 9$, $F_{\text{critical}} = 5.74$). To incorporate this characteristic scattering into our multiple property model, we define a differential scattering matrix, S, with s_{12} ($= s_{21}$) being the only nonzero term. Combining the normal optical properties embodied in H with the scattering properties in S, we arrive at

$$M = \exp(-H - S). \quad (5)$$

In this system, the s_{12} is a measure of the preferential polarized scattering, which is a function of scattering polar and azimuthal angle. The objective's numerical aperture (NA) determines the solid azimuthal angle of collected light that will contain contributions of the undeviated light and the preferentially polarized scattered light. The effective tissue culture medium scattering parameter, s_{12}, and CB were determined as a function of NA for our 4×, 10×, and 20× objectives and tabulated in Table 2. The physical significance of s_{12} will be addressed in the Discussion.

TABLE 2 Effective tissue culture medium s_{12} and CB for various numerical apertures

		medium	
Objective	NA	s_{12}	CB
4×	0.13	−0.057 ± 0.003	−1.38 ± 0.23
10×	0.30	−0.074 ± 0.003	−3.05 ± 0.18
20×	0.40	−0.080 ± 0.002	−4.63 ± 0.27

Linear birefringence

Although a sample's Mueller matrix may be uniquely determined, the combination of optical properties giving rise to that matrix is not unique (Schellman and Jensen, 1986). Therefore, to characterize the network alignment by its linear birefringence, the effective circular properties or scattering must be determined independently. This was accomplished by acquiring and fitting for the components of a sample of the same composition allowed to compact isotropically (hereafter referred to as the matched isotropic sample, meaning that the gel microstructure and thickness are matched, because we assume that the exact shape of the construct is unimportant.). Theory predicts that cell-driven compaction without a mechanical constraint does not yield network alignment (Barocas et al., 1998).

Matched isotropic sample

To build the complete optical model for the isotropic matched sample, optical and scattering parameters were added using the critical F-test criterion, described earlier. However, characterization of the matched isotropic sample includes not just scattering due to tissue-culture medium where the significance of s_{12} was originally demonstrated earlier, but also the scattering due to collagen. For thick samples, F-tests indicated that CB was often not a statistically significant parameter, but it will be included in our discussion for generality.

Rotating the sample under crossed polars confirmed that the sample was globally isotropic. MGL(θ) was fit to Eq. 1 to determine values for s_{12} and CB. Figure 4, *A* and *B* show the brightfield and s_{12} image for the matched isotropic

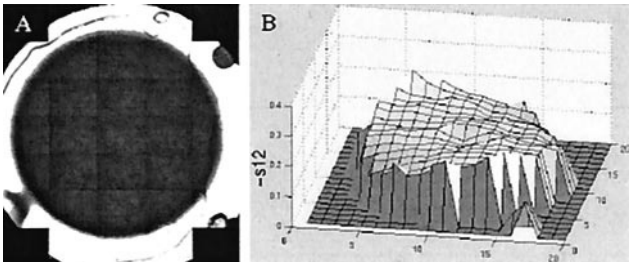

FIGURE 4 Brightfield and s_{12} images of an isotropic sample that has undergone about 20% compaction. (*A*) Brightfield image. (*B*) s_{12} Surface plot. The s_{12} surface is relatively flat, indicating a uniform scattering bias.

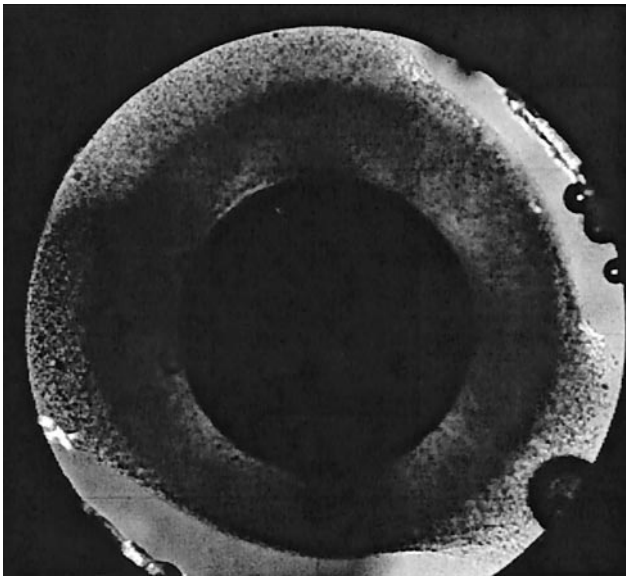

FIGURE 5 Polarized light image of a media-equivalent. The dark bands extending vertically and horizontally imply that collagen alignment is horizontal and vertical in the band regions, respectively. The bands were invariant to rotation of the ME, implying that alignment is circumferential.

sample that had undergone a similar amount of compaction (20%) to that of the aligned ME reported in the next section. The sample exhibited a uniform profile of s_{12}.

Media equivalent

After ~8 h compaction, the collagen network of the ME was aligned predominantly in the circumferential direction as shown by a crossed banding pattern under crossed polars in Fig. 5. Using the values for s_{12} and CB determined from the matched isotropic sample, the MGL(θ) data from 20 × 20 subregions of the ME were fit to Eq. 1 for the alignment direction and retardation (χ, δ). Following the F-test scheme, the data for each subregion were first fit using a scale and offset parameter, given the values for s_{12} and CB determined from the matched isotropic sample as estimates of the ME's parameters. Then, the data were fit for LB (two additional fit parameters, χ and δ). The F-test was used to reject linear retardations not statistically different from zero. Figure 6 shows vector maps of the alignment with alignment direction, χ, and magnitude proportional to the retardation, δ. Figure 6, *A* and *B*, correspond to regression results using the estimates of $s_{12} = 0$ (assuming no scattering) and $s_{12} = -0.17$, respectively. When we used no correction ($s_{12} = 0$), an alignment-directional bias toward $-45°$ was obtained.

The effects of s_{12} and CB estimates on the regression results can be seen in plots of the apparent LB parameters (χ_{app}, δ_{app}) versus s_{12} and CB in Fig. 7. Figure 7, *A* and *B*, show δ_{app} and χ_{app} for the matched isotropic sample. A true isotropic sample is characterized by (χ = undefined, $\delta = 0$),

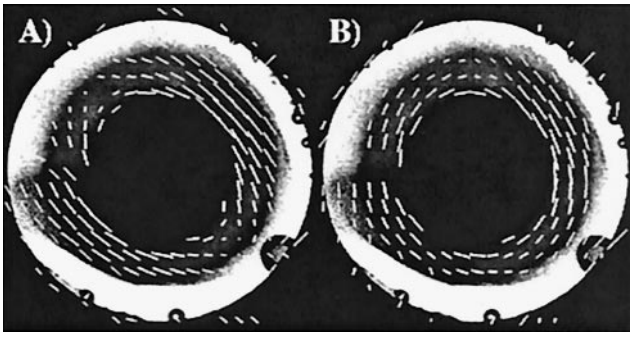

FIGURE 6 Alignment maps of a media-equivalent. Each white line indicates the local direction of alignment, and the length indicates the magnitude of the retardation. (*A*) Alignment map is not corrected for circular optical components and scattering. Note that there is a clear bias toward $-45°$. (*B*) Alignment map is corrected with $s_{12} = -0.17$.

and, therefore, the estimated scattering coefficient, $s_{12,o}$, and circular birefringence, CB_o, of the isotropic sample are the values where δ_{app} vanishes and χ_{app} becomes indeterminate. For our matched isotropic sample, this occurred at ($s_{12,o} = -0.17$, $CB_o = -10.3°$) as can be seen in Fig. 7, *A* and *B*.

In Fig. 7 *A*, δ_{app} varies hyperbolically with s_{12} and CB, with a strong dependence on s_{12}. In Fig. 7 *B*, a departure from ($s_{12,o}$, CB_o) yields a $\pm 45°$ bias in χ_{app} for large $s_{12,o}$ errors, and a 0° or 90° bias for a large CB_o error, depending on the sign of the s_{12} error. Note that assuming neither scattering nor CB (s_{12} = CB = 0) would lead to the nonsensical result of approximately ($\chi_{app} = -45°$, $\delta_{app} = 5°$), implying a spatially uniform alignment throughout the isotropic sample!

The effects of s_{12} and CB errors on the ME alignment map are shown in Fig. 7, *C* and *D*, for the northwest sector of the ME. Because of the known circumferential alignment, χ in this sector is approximately 45°. Uncorrected ($s_{12,o} = CB_o = 0$), $\chi_{app} \approx 90°$, but using $s_{12} = -0.17$, $CB_o = -10.3°$ from the matched isotropic sample, $\chi_{app} \approx 50°$, agreeing well with the known alignment in that sector. Similarly, s_{12} error resulted in a larger or smaller δ_{app} depending on where the sample alignment was parallel or perpendicular, respectively, to the bias direction as seen in the vector lengths of Fig. 6 *A*.

Error estimates

Accurate and precise measurement of light intensity is especially important in quantitative polarized light microscopy; therefore, understanding the effects of noise is critical to matters of sensitivity, accuracy, and precision. When not dealing exclusively in the low-light level regime, the photonic noise, or shot noise, is the most significant source of noise, and it is proportional to the square root of the number of photons. Simulations were performed to determine the

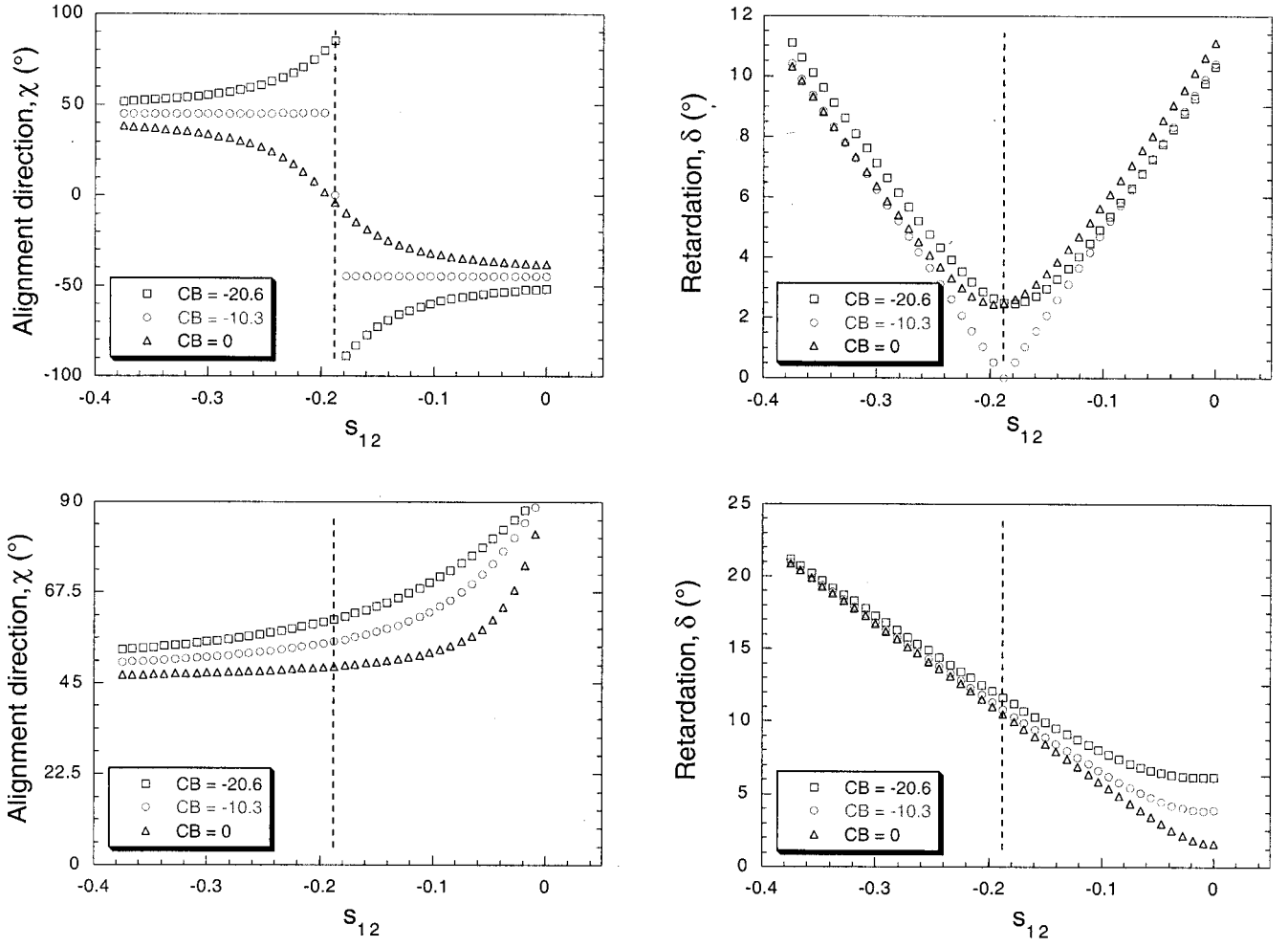

FIGURE 7 LB dependence on s_{12} and CB. (*A*, *B*) An isotropic sample. Note bias toward nonzero δ and $\chi = -45°$ when no scattering is assumed. (*C*, *D*) The NW region of the ME shown in Fig. 6, with approximate alignment of 45°. Vertical lines indicate the s_{12} where $\delta = 0$ for the isotropic sample.

effect of photonic noise on the estimated alignment direction (χ) and retardation (δ).

To assess whether errors were dependent on the sample alignment direction or magnitude, simulations were conducted with theoretical linear birefringent samples with alignment directions between 0 and 180° and retardations from 10^{-2} to 10^{2} degrees. Light intensity curves were generated from Eq. 1 and Gaussian noise was added, resulting in signal-to-noise ratios (SNR) between 10 and 10^4. Simulation results of photonic noise effects are shown in Fig. 8, *A* and *B*. The retardation error, ϵ_δ, and the error in the alignment direction, ϵ_χ, approximately follow, respectively;

$$\epsilon_\delta \propto \frac{1}{\mathrm{SNR}}, \tag{6}$$

$$\epsilon_\chi \propto \frac{1}{(\delta)(\mathrm{SNR})}. \tag{7}$$

For single-pixel full-well acquisition, the Kodak KAF 1400 camera achieves a photon-limited maximum SNR of about 200. This corresponds to a single-pixel retardation resolution of ~0.3° with a corresponding maximum error in alignment direction of $\epsilon_\chi = 4°$.

In practice, the matched isotropic sample may not have identical scattering properties to that of the aligned sample, an error in s_{12}, resulting in subsequent errors in δ and χ. Therefore, the effect of inaccurate correction of scattering bias was investigated by simulating sample scattering as $s_{12} = -0.1$ and SNR $= 10^3$ and determining (χ, δ) as a function of s_{12}. The effects of a 10% error in s_{12} and the assumption that there is no scattering ($s_{12} = 0$) are shown in Fig. 8, *C* and *D*.

Both ϵ_χ and ϵ_δ followed similar trends with increasing error in s_{12} as with increasing noise. For large s_{12} error, there is an apparent regression convergence to a nonzero retardation for vanishing true retardation (See Fig. 8 *C*). For large s_{12} error, the regression of any weakly aligned sample converged to a single sample-independent direction (as seen earlier in Fig. 7). The large error bars in Fig. 8 *D* are a result of this alignment-direction bias.

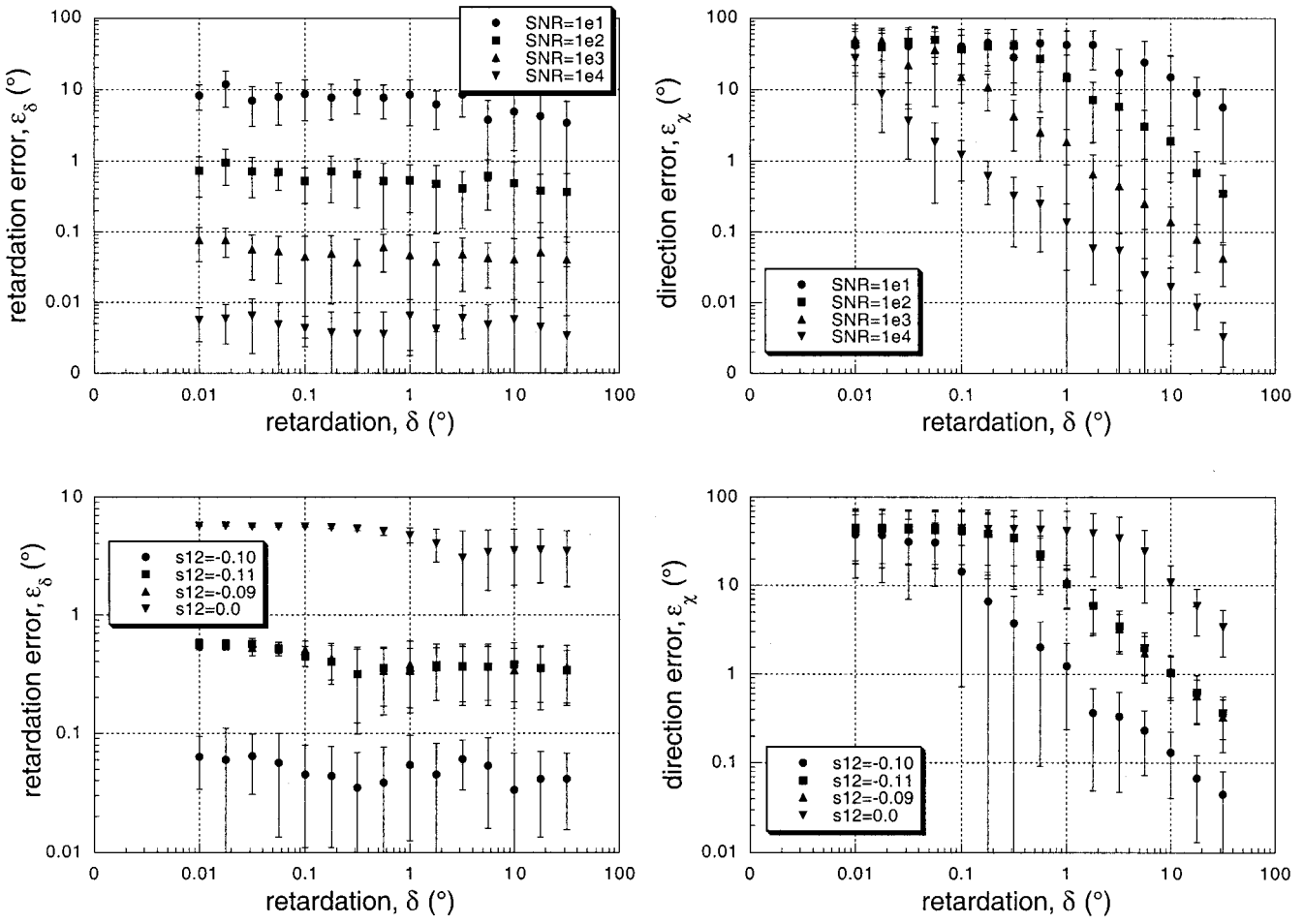

FIGURE 8 (*A*, *B*) Direction and retardation error, respectively, for accurate scattering estimate, s_{12} (= −0.10), and SNR, and (*C*, *D*) for fixed SNR (= 10^3) and varied s_{12}. Note the strong apparent retardation when ignoring scattering, similar to Fig. 7. The alignment direction error in these cases follows the same bias seen in Fig. 7.

DISCUSSION

Several difficulties arise from using a conventional light microscope for polarimetric studies. First, many microscopes, particularly inverted microscopes, are not equipped to handle the variety of rotating analyzer or post-specimen compensator methods, but instead are limited to a fixed analyzer and a slot beneath the objective. Consequently, to expand the capabilities of our existing workstation, we chose to adopt a method that interrogates the sample with a variety of polarization states using a polarization state generator, as coined by Hauge (1978), consisting of plane polarized light followed by a rotating λ/4 plate. This technique using a rotating λ/4 plate is, experimentally, much easier to implement than integration of sophisticated commercial photoelastic modulators, albeit one makes a significant sacrifice in speed of modulation. Moreover, by using a reference compensator plate on the sample stage, the optic train calibration determines the effective M_{LB} for misaligned and nonideal λ/4 plates.

The light intensity curves, $i(\theta)$, or, equivalently for 2D, the image sets, $I(\theta)$, contain information about the sample's Mueller matrices. Because the sample's linear, circular, and scattering properties cannot be uniquely determined simultaneously, the task was approached by first determining the CB and scattering (s_{12}) properties for a matched isotropic sample. Those values were then applied to the sample's differential Mueller matrices *H* and *S* and fit for the sample's LB. We were not interested in each element of the specimen's Mueller matrix per se, but only those pertaining to the measurement of LB, and the confounding circular and scattering properties. Hauge and others use a second rotating λ/4 plate for full determination of the Mueller matrix, but we have demonstrated that a fixed λ/4 plate aligned at 45° is sufficient for characterization of LB.

The effects of errors in s_{12} and CB on LB measurement as characterized by (χ, δ) for an aligned sample are shown in Fig. 7, *C* and *D*. Determination of the effective circular/scattering properties from a matched isotropic sample is

straightforward, because we define the effective s_{12} and CB as where χ = undefined, and $\delta = 0$ as shown in Fig. 7, *A* and *B*. This is the first application, to our knowledge, of circular/scattering component correction to the quantitative polarized light microscopy of tissues. Additionally, we find that biases in (χ, δ) due to s_{12} and CB decrease with increasing sample alignment as measured by δ.

The sensitivity of our method based on shot noise of the CCD imager is a retardation of ~0.3°, or ~0.5 nm, on a pixel-wise basis (Fig. 8). The SNR may be increased by binning pixels or integrating frames. Binning $n \times n$ pixels allows us to increase the SNR by a factor of n, and thus improve the minimum measurable retardation by a factor of n. The accuracy of the method is dependent on the SNR, and the degree to which s_{12} of the linear birefringent sample is properly matched. The calculated direction agrees well with the ME test case.

A major difficulty in using microscopes for polarimeters is that most polarimeters purposely only collect light from a very small angle ($\ll 2°$). This allows characterization of sample matrix elements as a function of scattering angle (Hunt and Huffman, 1973), or isolation of just the forward scattering where the scattering matrix is diagonal and characterized by three parameters. However, an objectives's numerical aperture, which determines the angle of light accepted into the imaging system, is about 7° for a 4× objective to 56+° for a high-power oil-immersion objective. Much of the scattered light is collected, with its altered polarization state, and must be accounted for in the analysis.

The s_{12} scattering was likely due to Rayleigh scattering off particles in the sample. The scattered light is s-polarized, that is, linear polarized normal to the scattering plane. The objective accepts light according to its numerical aperture, determining what scattering angles are collected. However, the rotating λ/4 plate method produces elliptically polarized light whose major axis is that of the polarizer transmission axis. The scattered light, therefore, also has a preferential polarization whose major axis is that of the polarizer. Because the s_{12} component represents a preferential absorption of linearly polarized light in the vertical or horizontal direction, a scattering polarization bias will be reflected in an effective absorption of the orthogonal component. Hence, using the polarizer and analyzer as our reference axes, this reflects why s_{12} is sufficient for characterization of the scattering properties of gels using this polarimetric approach. Many methods do not take polarized scattering into account, and may operate under false assumptions about the form of the sample's Mueller matrix, particularly in turbid media. However, certain polarimetric methods, such as those that use circularly polarized light (or small deviations from it), in the limit of measuring small retardations, would likely not suffer from these polarization biases because the scattering intensity would be isotropic, on average. Similarly, measuring weak retardations using a rotating polarizer method might avoid some of these problems because the scattered light would retain the same polarization sense as the incident light.

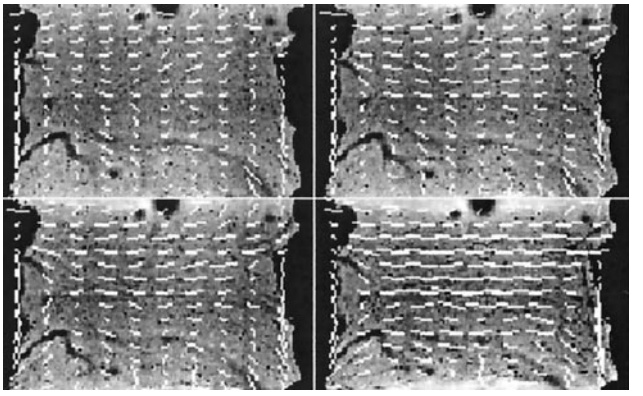

FIGURE 9 Isometric cell traction assay compaction time series. This time series over 15 h shows the development of alignment when the cell-induced compaction is constrained in the horizontal direction.

For the routine correction of scattering effects, one may be able to create a calibration curve of s_{12} versus sample thickness/density for different compositions. However, use of a matched isotropic sample is preferred. Even so, it is a first approximation of the correction, because it is likely that the alignment of the tissue fibers may perturb the polarization of the scattered light. Additionally, as the fiber diameter approaches the wavelength of light, scattering effects will become more complicated. We have intentionally used a very thick sample (0.5″) here to clearly demonstrate the importance of the scattering, and the broad utility of the method.

As is commonly the problem in biological polarization microscopy, the measured retardation gives an excellent semi-quantitative indicator of alignment, but because of form birefringence (arising from differing refractive indices of the sample's constituents, such as the collagen fibrils and interstitial cell culture medium in the ME) and the inherent scattering and multilamellar architecture in tissues, the intrinsic birefringence and related LB value is not generally obtained. However, our method can generate retardation maps of turbid gels that are indicative of the spatial variation of fiber alignment and hence instructive about the structure of the specimen. This is illustrated in Fig. 9, a series of alignment maps during cell-induced compaction of a cylindrical rod of collagen gel that is mechanically constrained at both ends (Knapp et al., 1999). At each time point, an increase in axial alignment is evident going from the ends toward the midplane of the rod.

Methods such as Oldenbourg's PolScope use simplifying assumptions appropriate for strict linear retarders having weak retardation to reduce the problem of LB determination to one of simple image operations, which allows huge computational savings. Although our method is not limited to low retardations, neither method, without the use of

additional wavelengths, can differentiate between retardation orders. However, this is generally not a limitation with respect to thin biological samples. Our method's key advantage is in the use of a more general model of the sample's optical properties to account for CB and scattering. As a result, our method is much more computationally intensive due to nonlinear regression. But, this allows for the characterization of thick samples in tissue culture medium, accounting for effects of scattering and circular properties on LB, and samples that do not act as strict linear retarders.

Many modern polarized light techniques require significant computer integration for specialized polarized light equipment (electro-optic modulators, lock-in amplifiers, etc.) which makes outfitting an existing microscope/image processing workstation often difficult or impractical. In our method, the measurement of birefringence is shifted from being dependent on such specific equipment to a computational problem, involving image analysis and least squares regression. A great advantage is that imperfect optical elements, such as nonideal $\lambda/4$ plates and the objective, can be accounted for accurately. The obvious disadvantage is computational time, which may be on the order of 5 min for a 20×20 grid map running on a Silicon Graphics O2. Clearly, fast computers will mitigate this disadvantage. Even with current computing speeds, using an adaptation of our method to tissues that are highly aligned such that scattering and CB can be neglected, pixel-wise LB maps (i.e., alignment images) can be generated in seconds (Tower and Tranquillo, 2001).

CONCLUSIONS

We have presented a novel methodology that greatly enhances the general-research light microscope/image analysis workstation by the ability to generate linear birefringence alignment maps of tissues or other anisotropic transparent materials that possess a degree of linear and circular optical properties and scattering effects. For a weakly aligned artificial tissue, a matched isotropic sample (or a calibration curve of the circular and scattering components of its constituents) can be used to correct for confounding optical properties, allowing determination of the alignment map. For strongly aligned native tissues, there is often no matched isotropic sample available; but, because the confounding effects of the scattering and circular properties tend to decrease with increasing linear birefringence, the effects can be neglected. Weakly aligned native tissues can be characterized as long as there is a portion of the sample that is isotropic for purposes of CB and scattering characterization (assuming CB and scattering do not vary spatially). Our methodology confers an elliptical polarimetry capability to an existing microscope/image analysis workstation with the addition of a few inexpensive optical components and straightforward nonlinear regression algorithms that account for nonidealities of optical components and determine the effective optical properties of aligned tissues and related complex tissue-like materials.

This work was supported by the Engineering Research Centers Program (EEC-8721551) of the National Science Foundation.

REFERENCES

Barocas, V. H., T. S. Girton, and R. T. Tranquillo. 1998. Engineered alignment in media equivalents: magnetic prealignment and mandrel compaction. *J. Biomech. Eng.* 120:660–666.

Bear, R. S., and F. O. Schmitt. 1936. The measurement of small retardations with the polarizing microscope. *J.O.S.A.* 26:363–364.

Brosseau, C. 1998. Fundamentals of Polarized Light: A Statistical Optics Approach. John Wiley & Sons, Inc., New York.

Finzi, L., L. Ulibarri, and C. Bustamante. 1991. Differential polarization imaging: V. numerical aperture effect and the contribution of preferential scattering and absorption to the circular dichroism images. *Biophys. J.* 59:1183–1193.

Geday, M. A., W. Kaminsky, J. G. Lewis, and A. M. Glazer. 2000. Images of absolute retardance $L \cdot \Delta n$, using the rotating polariser method. *J. Microscopy.* 198:1–9.

Glazer, A. M., J. G. Lewis, and W. Kaminsky. 1996. An automatic optical imaging system for birefringent media. *Proc. Roy. Soc. Lond. (A).* 452:2751–2765.

Guido, S., and R. T. Tranquillo. 1993. A methodology for the systematic and quantitative study of cell contact guidance in oriented collagen gels. Correlation of fibroblast orientation and gel birefringence. *J. Cell Sci.* 105:317–331.

Hauge, P. S. 1978. Mueller matrix ellipsometry with imperfect compensators. *J. Opt. Soc. Am.* 68:1519–1528.

Hennessey, J. P., Jr., and W. C. Johnson, Jr. 1982. Experimental errors and their effect on analyzing circular dichroism spectra of proteins. *Anal. Biochem.* 125:177–188.

Hunt, A. J., and D. R. Huffman. 1973. A new polarization-modulated light scattering instrument. *Rev. Sci. Instrum.* 44:1753–1762.

Jones, R. C. 1948. A new calculus for the treatment of optical systems. VII. Properties of *n*-matrices. *J. Opt. Soc. Am.* 38:671–685.

Kim, M., D. Keller, and C. Bustamante. 1987. Differential polarization imaging: I. Theory. *Biophys. J.* 52:911–927.

Knapp, D. M., T. T. Tower, R. T. Tranquillo, and V. H. Barocas. 1999. Estimation of cell traction and migration in an isometric cell traction assay. *AICHE J.* 45:2628–2640.

Long, M. M., and D. W. Urry. 1981. Absorption and circular dichroism spectroscopies. *Mol. Biol. Biochem. Biophys.* 31:143–71. Review.

Oldenbourg, R., and G. Mei. 1995. New polarized light microscope with precision universal compensator. *J. Microscopy.* 180:140–147.

Osaki, S. 1994. A new method for the determination of polymer optical anisotropy. *J. Appl. Phys.* 76:4323–4326.

Schellman, J., and H. P. Jensen. 1986. Optical spectroscopy of oriented molecules. *Chem. Rev.* 87:1359–1399.

Thomsen, S., J. A. Pearce, and W. F. Cheong. 1989. Changes in birefringence as markers of thermal damage in tissues. *IEEE Trans. Biomed. Eng.* 36:1174–1179.

Tower, T. T., and R. T. Tranquillo. 2001. Alignment maps of tissues: II. Fast harmonic analysis for imaging. *Biophys. J.* 81:2964–2971.

van de Hulst, H. C. 1957. Light Scattering by Small Particles. General Publishing Company, Ltd., Toronto, Canada.

van Haeringen, B., J. P. Dekker, M. Bloemendal, M. Rogner, R. van Grondelle, and H. van Amerongen. 1994. Simultaneous measurement of electric birefringence and dichroism. A study on photosystem 1 particles. *Biophys. J.* 67:411–417.